Medical Engineering and Physics 71 (2019) 3–9

Contents lists available at ScienceDirect

Medical Engineering and Physics

journal homepage: www.elsevier.com/locate/medengphy

Development of a simplified, reproducible, parametric 3D model of the talus

Haihua Ou[a], Jialiang Su[a], Shouren Lan[b], Lisheng Wang[b], Xiangyang Xu[c,*], Shane Johnson[a,d,*]

[a] University of Michigan and Shanghai Jiao Tong University Joint Institute, Shanghai Jiao Tong University, Shanghai, China
[b] Department of Automation, Institute of Image Processing and Pattern Recognition, Shanghai Jiao Tong University, Shanghai, China
[c] Ruijin Hospital, Shanghai Jiao Tong University School of Medicine, Shanghai, China
[d] State Key Laboratory of Mechanical System and Vibration, Shanghai Jiao Tong University, Shanghai, China

ARTICLE INFO

Article history:
Received 7 September 2018
Revised 27 March 2019
Accepted 9 June 2019

Keywords:
Computed tomography
Talus
Shape fitting
Optimization
Auto meshing

ABSTRACT

Computational foot models have significant application in surgical decision making, injury and disease diagnosis and prevention, sports performance analysis and footwear engineering. However, due to the substantial time in model building and the heavy computational costs from the complexity of the models, daily clinical application of these foot models has yet to be achieved. Much of the previous research adopted a detailed-geometry approach in modeling bones that potentially contributed to the heavy computational costs. In this research, we developed a computational talus model based on CT section image data, image reconstruction and segmentation, contact surface identification, standard shape fitting, and finite element auto meshing algorithms. Modeling the bones as rigid is common, and modeling the contact surfaces only for the rigid body saves additional computational resources. Priority, therefore, in the shape fitting with optimization is given to the contact surfaces of the talus. Thirteen sets (9 males and 4 females) of CT section data were obtained. Image reconstruction, segmentation and bone labeling were conducted on each set of CT data to identify talus and its adjacent bones. Contact surfaces of the talus were then identified based on bone spatial relationships. Apart from the talar dome surface which was fitted by a 3rd-order polynomial, standard shapes such as ellipsoids and planes were used to fit the selected contact surfaces so that the geometrical parameters maintain physical significance. Based on these parameters, we automatically recreated and meshed the least-squares fitted shapes rapidly with limited elements. Last, mean major contact surfaces of the talus were obtained and fitted by standard shapes. Although the number of samples in this study was relatively small, our method provides sufficient and accurate geometric parameters of these contact surfaces to completely describe and reproduce the talus, on both a subject specific and average basis. The method for describing the talus here helps to parametrize computational models using planes and ellipsoids, improves surgical decision making and implants with a more precise and physically significant measures, and the description provides bone geometric parameters which can later be used to relate risk analysis for bone shape specific injury rates.

1. Introduction

The human foot and ankle is a flexible structure with complex coupled kinematic motions including internal/external rotation, dorsiflexion/plantar flexion and inversion/eversion [1]. In stance and gait, it supports the whole body and experiences frequent impact forces which brings a high risk of injury. For example, 26.2% military recruits sustains at least one foot and ankle injury during basic military training in the armed forces [2]. Finite element (FE) models of foot and ankle have been developed for analyzing pathological conditions and designs of foot orthoses [3–8]. Despite its development over the years, to the authors' knowledge, daily clinical application of these FE models has not been achieved. Efforts towards this goal need to be made in reducing 1) substantial time in model building, and 2) heavy computational costs due to the complexity of the models.

The geometry of the talus is a key component in foot and ankle modeling. In describing the morphology of the talus, 3D FE models typically adopt a detailed-geometric approach [3,6,8]. In this approach, to achieve the realistic and computational

* Corresponding authors.
E-mail addresses: xu664531@hotmail.com (X. Xu), shane.johnson@sjtu.edu.cn (S. Johnson).

https://doi.org/10.1016/j.medengphy.2019.06.022
1350-4533/

models of the entire foot, more than 30,000 8-node hexahedral elements were needed [9,10]. Further, no parametric information can be obtained for bones, limiting the potential to understand the relation between bony structure and functional performance of the foot and ankle or to conduct inter-person comparisons when interpreting model results. On the other hand, the development in morphometry analysis of the talus [11–22] may push forward the parameterization of the talus. Some methods require a significant amount of manual process, e.g., measurement of cadaveric samples [14], manual thresholding process for bone segmentation [16] or manual selection of articular surfaces [15]. The need for excessive time and expertise personnel in these methods limit their potential in large-scale subject specific applications. More recently, statistical shape modeling (SSM) was largely utilized to model the geometrical variations of bones/organs. Given a set of image data, typical steps in SSM include placing landmarks on each sample, establishing correspondence between landmarks from different samples, aligning/normalizing each sample to their mean, and applying principal component analysis (PCA) to identify the major modes of intra-class variations and obtain a succinct and parametric way to represent the original geometry [17]. SSM has been applied in generating patient-specific or statistical models for bones such as the femur [18], the first metatarsal [13], the clavicle [19], for skeletal structure such as the ribcage [20] and for organs such as the liver [21]. It has also been applied in detecting localized changes of mechanical properties in muscles [22]. Generally, the SSM method is powerful and capable of accurately describing the geometry, and can reveal the principal modes of variations. Despite that SSM presents a general, accurate and parametric approach to model the talus, it adopts a detailed-geometry approach that could significantly increase computational costs. If SSM is adopted, surface region selections and this potential geometric perturbation must still be conducted for contact interfaction specifications. Some studies have been conducted on specific sections or regions of the talus. For example, the talar dome surface was selected and fitted by a bi-truncated cone [12]. An experimental technique using ankle artificial approximation based on the saddle-shaped truncated cone concept was also developed [11]. The talonavicular joint morphology has been parameterized and compared for different foot types [15,16]. These morphological studies provide insight into the correlations between geometry of particular articular surfaces and pathological conditions such as flat foot. However, the investigated morphological parameters of the articular surfaces provided mostly general descriptions such as the length of the articular surfaces, instead of detailed descriptions of the entire surface shape, which is important in finite element studies when joint pressure is concerned. Further, other articular surfaces of talus are equally important in the foot and ankle structure and predicted function, and geometry of different articular surfaces of the talus has not been considered together previously.

The purpose of our study is to develop a simplified parametric talus model based on CT section image data, standard shape fitting, and finite element auto-meshing algorithms. The developed talus model can be beneficial for subject-specific FE modeling, medical visualization, such as targeted diagnosis and for understanding the relation between bony structure and performance of foot and ankle. Since the modulus of the bones is significantly higher than ligaments, soft tissue, etc. [3,23], the foot bones can be considered rigid in static and dynamic analysis. Articular surface features then are dominate parameters of the model analysis given the rigid body assumption until fracture. In this study, therefore, only the contact surfaces are modelled for bones, which saves computational resources. We also use standard shapes such as ellipsoids and planes to fit our selected contact surfaces so that the geometrical parameters maintain physical significance. Finally, based on these parameters, we automatically meshed the least-squares fitted shapes and rapidly developed a 3D simplified finite element parametric talus.

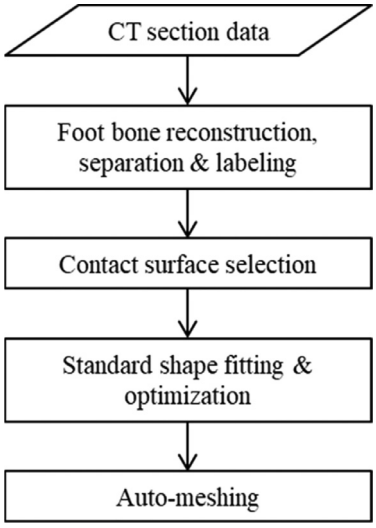

Fig. 1. Flow chart of the methodology in this study.

2. Materials and methods

The flow chart of the methodology in this study is shown in Fig. 1. Informed consent in accordance with the Declaration of Helsinki was obtained from each participant prior to the start of the study. CT section scanning was first performed on the foot and ankle of each subject. Based on the obtained CT section data, foot bones were reconstructed and segmented using an in-house software [24] and each individual bone was labeled automatically. Contact surfaces of the talus were identified and fitted with standard shapes including ellipsoid and plane. After the fitting, an auto-meshing algorithm was used to mesh the contact surfaces. Finally, by repeating the previous methodology for all the subjects, an average description of the talus was obtained.

2.1. Data acquisition

In this study, 13 sets of CT section data (9 males and 4 females from 23 to 46 years old) were obtained. At the time of scanning, foot and ankles of the subjects reflected no abnormal or pathologic characteristics. CT examination was performed on a 64-slice multi-detector CT scanner (Sensation 64, SIEMENS, German), with a 50 cm scan field of view, a 1.0 mm slice thickness and 0.4023 mm pixel spacing acquisition, 120 kVp and 136 mA X-ray tube current.

2.2. Foot bones reconstruction, separation and labelling

The foot bones were reconstructed by the Volrendering software, which was developed by the authors and based on the improved 2D transfer function [24]. The reconstruction process includes image denoising, scalar value and gradient magnitude (SG-TF) confirmation, spatial connectivity computation and attributes identification. Specifically, spatial positions of bone boundaries and their regions in the SG-TF space are computed, from which boundaries can be separated. The boundaries are divided into three classes and different boundary separation techniques are applied to them respectively. An example of the separated foot bones is shown in Fig. 2. After separation, the whole foot was then rotated and translated to get a unified Cartesian coordinate system,

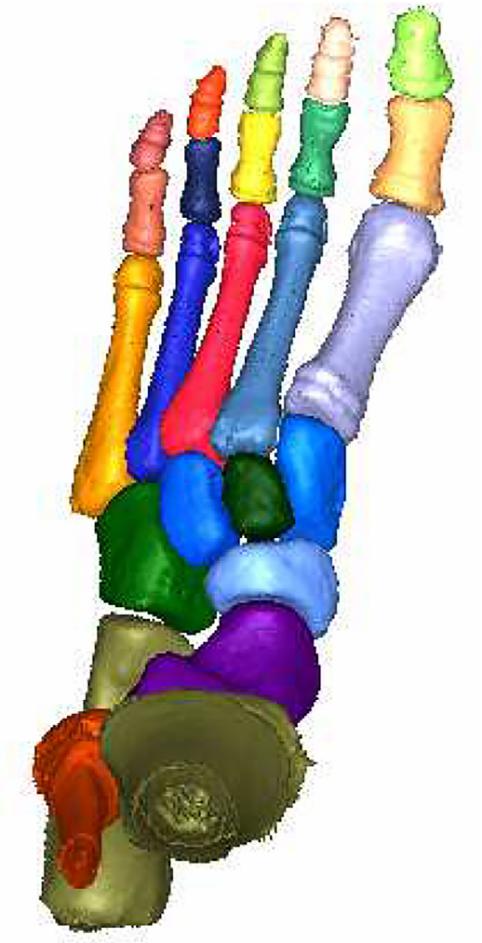

Fig. 2. An example of separated foot bones (color in print).

as shown in Fig. 3. The talus and fibula were first labeled from the bones based on the z values. Starting from the proximal to distal end of the foot, other bones are labeled based on their spatial relationship and using the 'Find Nearest Algorithm' [25].

2.3. Contact surface selection

There are five main contact surfaces between the talus and adjacent bones: talus superior surface (between the talus and the tibia), talus-fibula surface, talus head (between the talus and the navicular) and talus-calcaneus I (proximal) and talus-calcaneus II (distal) [14]. For finding these five contact surfaces, we divided the whole process into two steps: rough and refined selections. The rough selection was based on bone spatial relationships. The central points of the tibia, calcaneus and navicular were utilized to find the superior, inferior and head surface of the talus, respectively. The fibula's nearest point with the talus was found to define the talus-fibula contact surface. In this unified global coordinate system, the point with the minimal x-axis value on the calcaneus can be utilized to define the talus-calcaneus II surface. After the rough selection, some coordinate values comparisons were performed in the refined selection. As shown in the Fig. 4, rough surfaces (green points) were first selected using the position of the centroid of the tibia. Then upper points (red ones) were selected by choosing minimal z-axis values in this current unified global coordinate system. The refined selection of other talus surfaces also followed the same methodology.

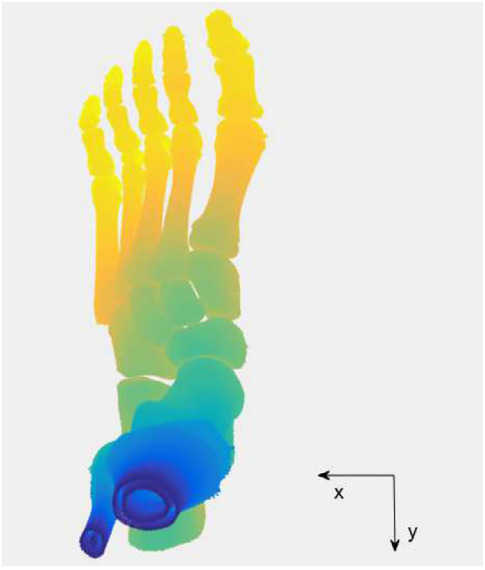

Fig. 3. Unified global coordinate system.

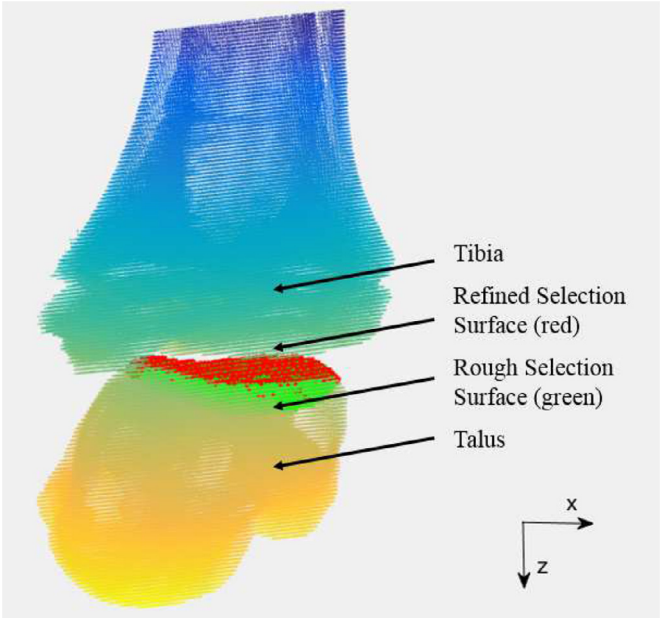

Fig. 4. Diagram of rough and refined surface selection (color in print).

2.4. Standard shape fitting and optimization

After obtaining the refined contact surface of the talus, we used the least square algorithm to select the best shape from standard shapes, including ellipsoids and planes to fit the contact surfaces, respectively. The ellipsoid fitting function is shown in (2.1).

$$Ax^2 + By^2 + Cz^2 + 2Dxy + 2Exz + 2Fyz + 2Gx + 2Hy + 2Iz = 1 \tag{2.1}$$

The center, radii and the eigenvectors of the fitted ellipsoid were then determined.

For plane fitting, the singular value decomposition (SVD) method was used to obtain the plane normal vector which can be represented as A, B, C and D in the plane Eq. (2.2). The least squares criterion was also used to find the best-fit plane.

$$Ax + By + Cz + D = 0 \tag{2.2}$$

The least square results obtained from ellipsoid and plane fitting were compared again to determine the final shape representation.

However, there is a special case among these contact surfaces. The talus superior surface is quite complicated (having multiple reversed curvatures). Fitting with standard shapes (i.e. ellipsoids and planes) would result in large errors or multiple piecewise discontinuous representations. To overcome this problem, we fit a surface function (2.3) for a parametric representation of talus superior surface.

$$f(x,y) = p00 + p10 \times x + p01 \times y + p20 \times x^2 + p11 \times x \times y + p02 \times y^2 + p30 \times x^3 + p21 \times x^2 \times y + p12 \times x \times y^2 + p30 \times y^3 \quad (2.3)$$

2.5. Auto-meshing

Based on the parameters from standard shape fitting, an auto-meshing algorithm was utilized to generate a mesh of the contact surfaces of the foot bones [26]. The geometry of the contact surface was described implicitly by its distance function. The distance function of the ellipsoid can be described by Eq. (2.4). Points are represented as p, and the radius of the ellipsoid in x, y, and z axis are represented as a, b and c, respectively. The ellipsoid centroid here was set at the origin in the Cartesian coordinate system. The ellipsoid mesh was then translated and rotated according to the centroid and eigenvectors obtained from the standard shape fitting. The distance function of the plane was set as (2.5), where x_1, x_2, y_1 and y_2 are the rectangle boundaries. The plane mesh was generated in the original position and direction. Then the plane mesh was translated and rotated according to the center and direction obtained from the shape fitting.

$$f_d = \frac{p_x^2}{a^2} + \frac{p_y^2}{b^2} + \frac{p_z^2}{c^2} - 1 \quad (2.4)$$

$$f_d = -\min(\min(\min(-y_1 + p_y, y_2 - p_y), -x_1 + p_x), x_2 - p_x) \quad (2.5)$$

The edge length of the mesh is adjustable, and uniform mesh was consistently applied throughout the process.

2.6. Average main contact surfaces of the talus

The average talus head, talus-calcaneus I and talus superior surface geometric descriptions were obtained in the following method. The point cloud data of each contact surface was re-sampled in MeshLab [27], using a Poisson's disk sampling to achieve a more uniform distribution of points. After that, surface registration was performed between contact surfaces from different samples using the iterative closest point (ICP) algorithm. A sphere was fit to all registered surfaces. The fitted sphere was segmented based on the zenith and normal angles. The average contact surface was obtained by calculating the mean coordinates of points lying in each segmented piece. Last, the average talus head and talus-calcaneus I surface were fitted by the ellipsoid function again.

3. Results

The talus contact surface geometry selected and refined by our algorithms are shown in Fig. 5. The average contact surfaces of the talus are shown in Fig. 6. The mean, standard deviation and maximum of the fitting errors for a sample set, all sample sets and

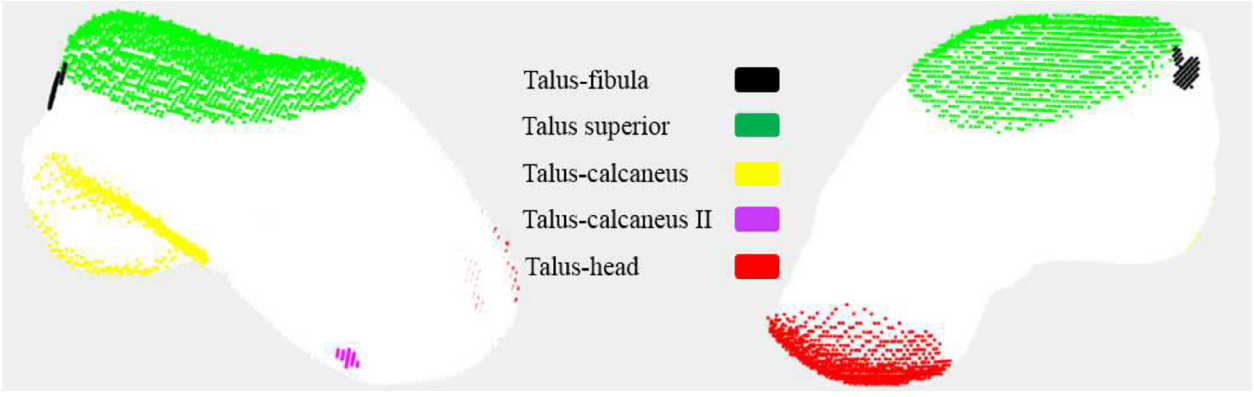

Fig. 5. Refined contact surfaces of the talus (color in print).

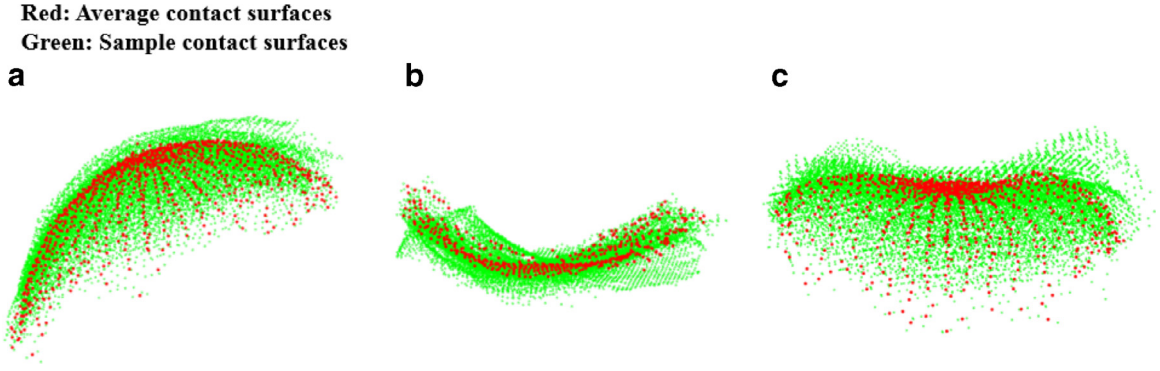

Fig. 6. Talus contact surface series: (a) talus head; (b) talus-calcaneus I; (c) talus superior. (color in print).

Table 1
Mean, standard deviation and max of error between the fitted and actual shape of the talus from the 1st set of data (unit: mm).

Contact surface	Fitting type	Mean	Standard deviation	Max
Talus head	Ellipsoid	1.21	0.72	3.30
Talus-calcaneus I	Ellipsoid	1.85	1.16	4.45
Talus-calcaneus II	Plane	0.22	0.11	0.55
Talus-fibula	Plane	0.20	0.14	0.61
Talus dome	3rd-order polynomial	0.81	0.55	2.26

Table 2
Mean, standard deviation and max of error between the fitted and actual shape of the talus from 13 sets of data (unit: mm).

Contact surface	Fitting type	Mean	Standard deviation	Max
Talus head	Ellipsoid	1.17	0.96	6.82
Talus-calcaneus I	Ellipsoid	1.40	1.06	5.24
Talus-calcaneus II	Plane	0.16	0.15	0.67
Talus-fibula	Plane	0.19	0.14	0.72
Talus dome	3rd-order polynomial	0.92	0.71	4.90

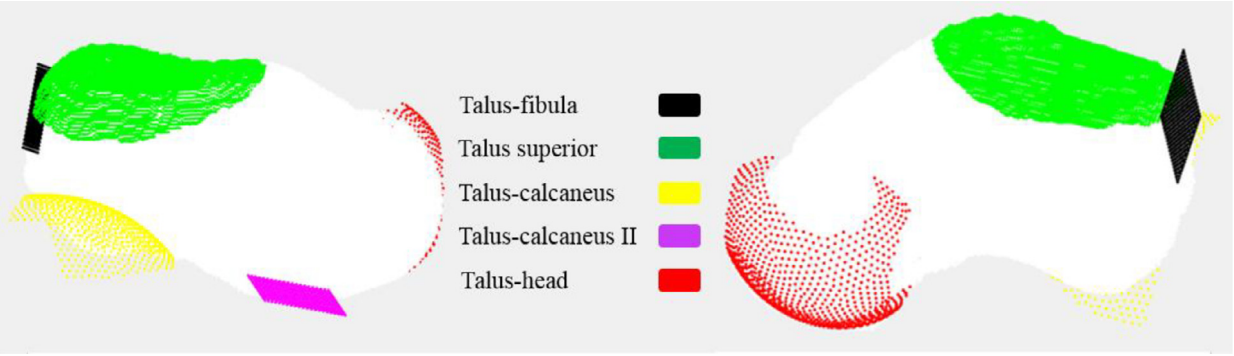

Fig. 7. Meshing nodes of the talus contact surfaces.

Table 3
Mean, standard deviation and max of error between the fitted and actual shape of the mean talus head and talus-calcaneus I (unit: mm).

Contact surface	Fitting type	Mean	Standard deviation	Max
Talus head	Ellipsoid	0.46	0.27	1.48
Talus-calcaneus I	Ellipsoid	1.63	0.77	3.10

the average contact surfaces of the talus are shown in Table 1, Table 2 and Table 3 respectively. Detailed fitting parameters including the centroid and radius for the ellipsoids are provided in Tables A.1 and A.2 in Appendix A. In Fig. 7, the auto-meshing nodes are shown based on the best-fit geometric parameters.

4. Discussion

A precise description of foot bone geometry is critical for targeted ankle-related diagnosis, surgeries and orthotic intervention. As an example, implant geometry used in the orthopaedic ankle-related surgery commonly relies on a simple generic template, whose shape may not be compatible with ankle bones and ligaments structures [12,28]. Even slight differences between natural and implanted bones will cause deterioration and poor outcomes [1,28].

The method used in this research to build the talus model is of sufficient accuracy. Parameters of each contact surface of the talus were obtained by standard shape fitting or surface fitting functions. Ellipsoid and plane fitting deviation results were compared in the optimization step. The shape with less deviation was returned as the output. If the difference of the deviation is small, the method preferred to return plane as the output as the plane has less parameters and complexity. Based on the low deviation, the geometric parameters listed in the result tables are acceptable in surgical applications and development of foot and orthotic models. Based on these 13 talus samples, we also developed an average talus model defined by its main contact surfaces. Researchers may refer to this average talus for comparative purposes or for the development of a standard or generic template for the talar implants, for example, especially when subject specific contact surface information is unavailable. Notice that although the mean deviation of the fitted talus superior surface as shown in Table 2 is significantly larger than that in Huang's work, in which bi-truncated cone (discontinuous surface) was fitted and its mean deviation is around 0.36 [12], the fitting function in this study provides a continuous description for the talus superior surface.

Despite its accuracy, the method in this research is also automatic, simplified and parametric, which makes it promising for large-scale subject specific FE modeling and correlating bony structure and risk of injuries/pathological conditions. First, the raw CT data was obtained to reconstruct the foot bones. The foot bones were separated automatically using our improved 2D transfer function. Compared with the method reported by Camacho and colleagues [29], our process requires no manual tasks, such as the

"bones border delineation" [29]. The talus can be obtained from the bone segmentation, and its contact surfaces were identified automatically, which reduces the need for excessive time and expertise compared to manual selections [15]. Compared to the contact surface selection method based on curvature of the surface and manual thresholding [16], the contact surface selection algorithm in this study is based on the relative position of the bones, so it is a general and robust methodology such that its application can be extended to other foot bones. Meanwhile, the area of each contact surface is adjustable which makes this algorithm more adaptive. The representation of relatively rigid bones by their contact surfaces reduces the number of elements needed compared with other FE foot bone models which generated the mesh based on the exact geometry from the CT scan [3,6,8] and patient-specific bone models based on SSM [13,18]. Thus, building time is reduced and computational costs are saved. Compared with another simplification scheme of the foot bony structure, where metatarsals were represented by spheres and cylinders [30], the method in this study is more general such that it can be applied for bones with more complex geometries. The automatic and simplified features of the method make it promising for large-scale subject specific FE modeling. Further, parameterization of most contact surfaces are based on standard shape fitting technique. The geometric parameters of the contact surfaces maintain physical meaning, similar to Sarrafian's anatomic descriptions [14]. The ellipsoid radius can be utilized to quantitatively reflect the curvatures of the contact surfaces. In future work, these geometric parameters can further be analyzed by statistical methods to research relationships between shape and injury or disease, such as flat foot [15,16]. Finally, there are a few limitations of the current study. It should be noticed that only 13 sample data are considered in this study and they are from a limited age range and a limited ethnic group (Chinese). Therefore, it may not serve as a global average. Since the bony structure is represented by contact surfaces only, abnormality locating outside of the contact surfaces would be excluded from the analysis. Further, the rigid body assumption of bones would prevent the analysis of pathological conditions such as stress fractures. A smarter and problem-based simplification scheme needs to be developed such that more details are considered close to the domain of interest. In terms of the contact surfaces, localized deviation was induced during parameterization and may cause error in analyzing joint pressure. A weighted fitting scheme, enforcing perfect fitting in critical locations on contact surfaces, needs to be developed to further reduce errors. Further, the current choices of standard shapes, i.e. ellipsoids and planes, may not be feasible for complex contact surfaces, as witnessed in the case of talar dome. Applying principal component analysis to the extracted contact surfaces can be a more general solution. The proposed method, however, presents a computationally efficient approach to simplify ellipsoid/plane-like contact surfaces which is good for selection and specification of contact interactions.

5. Conclusions

We developed a computational parametric talus model based on CT section image data, standard shape fitting, and finite element auto meshing algorithms. An average talus model is also provided describing the contact surfaces. Given a rigid body assumption, only contact surfaces of the talus are considered. Standard shape fitting of these contact surfaces provides geometric parameters with acceptable deviations. These parameters maintain accurate physical meaning and can be utilized to reconstruct the talus.

Conflicts of interest

All authors do not have conflicts of interest in this work.

Ethical approval

The authors confirmed that "The collection and use of the CT data on which this study was based adhered to the institutional policies and procedures of Ruijin Hospital, Shanghai Jiao Tong University School of Medicine. The study was approved by the ethics committee of Ruijin Hospital, Shanghai Jiao Tong University School of Medicine, and informed consent was obtained from each participant prior to the start of the study.

Acknowledgments

This research was supported by State Key Laboratory of Mechanical System and Vibration at Shanghai Jiao Tong University and National Science Foundation of China funding under Grant nos. 51505282, 51550110233, and 51750410692.

Appendix A

The centroids of the fitting ellipsoids are provided to locate the position of the corresponding shapes in the form of the coordinate values. The radius and corresponding radii direction vector are provided to determine the ellipsoid size and direction.

Table A.1
Geometric parameters of a sample set of data obtained from shape fitting and optimization (Unit: mm).

Contact surface	Fitting type	Centroid (x,y,z)	Radius (a,b,c)	Vector (matrix)/ Para (A,B,C,D)
Talus head	Ellipsoid	219.19 415.93 18.70	26.29 20.55 20.17	0,1,0; 0,0,1; 1,0,0;
Talus-calcaneus I	Ellipsoid	249.93 358.71 32.65	35.37 25.99 25.99	0,1,0; 1,0,0; 0,0,1;
Talus-calcaneus II	Plane	/	/	−2457.95 −0.58 7.49 −5.84
Talus-fibula	Plane	/	/	2009.03 −9.31 1.05 1.65

Table A.2
Geometric parameters of the average talus contact surfaces obtained from shape fitting and optimization (Unit: mm).

Contact surface	Fitting type	Centroid (x,y,z)	Radius (a,b,c)	Vector(matrix)/ Para (A,B,C,D)
Talus head	Ellipsoid	−16.805 −26.573 21.474	26.257 23.110 23.140	1,0,0; 0,1,0; 0,0,1;
Talus-calcaneus	IEllipsoid	36.483 45.577 7.420	40.120 40.120 40.120	1,0,0; 0,1,0; 0,0,1;

References

[1] Koh JL, Wirsing K, Lautenschlager E, Zhang LO. The effect of graft height mismatch on contact pressure following osteochondral grafting - A biomechanical study. Am J Sports Med 2004;32:317–20.

[2] Psaila M, Ranson C. Risk factors for lower leg, ankle and foot injuries during basic military training in the maltese armed forces. Phys Ther Sport 2017;24:7–12.

[3] Cheung JTM, Zhang M. A 3-dimensional finite element model of the human foot and ankle for insole design. Arch Phys Med Rehabil 2005;86:353–8.

[4] Erdemir A, Saucerman JJ, Lemmon D, Loppnow B, Turso B, Ulbrecht JS, et al. Local plantar pressure relief in therapeutic footwear: design guidelines from finite element models. J Biomech 2005;38:1798–806.

[5] Erdemir A, Viveiros ML, Ulbrecht JS, Cavanagh PR. An inverse finite-element model of heel-pad indentation. J Biomech 2006;39:1279–86.

[6] Gefen A, Megido-Ravid M, Itzchak Y, Arcan M. Biomechanical analysis of the three-dimensional foot structure during gait: a basic tool for clinical applications. J Biomech Eng-Trans ASME 2000;122:630–9.

[7] Goske S, Erdemir A, Petre M, Budhabhatti S, Cavanagh PR. Reduction of plantar heel pressures: insole design using finite element analysis. J Biomech 2006;39:2363–70.

[8] Guiotto A, Sawacha Z, Guarneri G, Avogaro A, Cobelli C. 3D finite element model of the diabetic neuropathic foot: a gait analysis driven approach. J Biomech 2014;47:3064–71.

[9] Chokhandre S, Halloran JP, van den Bogert AJ, Erdemir A. A three-dimensional inverse finite element analysis of the heel pad. J Biomech Eng-Trans ASME 2012;134.

[10] Fontanella CG, Matteoli S, Carniel EL, Wilhjelm JE, Virga A, Corvi A, et al. Investigation on the load-displacement curves of a human healthy heel pad: in vivo compression data compared to numerical results. Med Eng Phys 2012;34:1253–9.

[11] Belvedere C, Siegler S, Ensini A, Toy J, Caravaggi P, Namani R, et al. Experimental evaluation of a new morphological approximation of the articular surfaces of the ankle joint. J Biomech 2017;53:97–104.

[12] Huang J, Liu H, Wang D, Griffith JF, Shi L. Talar dome detection and its geometric approximation in CT: sphere, cylinder or bi-truncated cone? Comput Med Imaging Graph 2017;57:62–6.

[13] Scarton A, Sawacha Z, Cobelli C, Li X. Towards the generation of a parametric foot model using principal component analysis: a pilot study. Med Eng Phys 2016;38:547–59.

[14] Kelikian AS, Sarrafian SK. Sarrafian's anatomy of the foot and Ankle: descriptive, topographic, functional. Wolters Kluwer Health/Lippincott Williams & Wilkins; 2011.

[15] Louie PK, Sangeorzan BJ, Fassbind MJ, Ledoux WR. Talonavicular joint coverage and bone morphology between different foot types. J Orthop Res 2014;32:958–66.

[16] Peeters K, Schreuer J, Burg F, Behets C, Van Bouwel S, Dereymaeker G, et al. Alterated talar and navicular bone morphology is associated with pes planus Deformity: a CT-Scan study. J Orthop Res 2013;31:282–7.

[17] Sarkalkan N, Weinans H, Zadpoor AA. Statistical shape and appearance models of bones. Bone 2014;60:129–40.

[18] Grassi L, Schileo E, Boichon C, Viceconti M, Taddei F. Comprehensive evaluation of PCA-based finite element modelling of the human femur. Med Eng Phys 2014;36:1246–52.

[19] Lu Y-C, Untaroiu CD. Statistical shape analysis of clavicular cortical bone with applications to the development of mean and boundary shape models. Comput Methods Programs Biomed 2013;111:613–28.

[20] Wang Y, Cao L, Bai Z, Reed MP, Rupp JD, Hoff CN, et al. A parametric ribcage geometry model accounting for variations among the adult population. J Biomech 2016;49:2791–8.

[21] Lu Y-C, Untaroiu CD. A statistical geometrical description of the human liver for probabilistic occupant models. J Biomech 2014;47:3681–8.

[22] Leineweber M, Gao Y. Examining the feasibility of applying principal component analysis to detecting localized changes in mechanical properties. J Biomech 2015;48:262–8.

[23] Behforootan S, Chatzistergos P, Naemi R, Chockalingam N. Finite element modelling of the foot for clinical application: a systematic review. Med Eng Phys 2017;39:1–11.

[24] Lan S, Wang L, Song Y, Wang Y-P, Yao L, Sun K, et al. Improving separability of structures with similar attributes in 2D transfer function design. IEEE Trans Vis Comput Graph 2017;23:1546–60.

[25] Muja M, Lowe DG. Fast approximate nearest neighbors with automatic algorithm configuration. In: Proceedings of the fourth international conference on computer vision theory and applications., 1; 2009. p. 331–40.

[26] Persson PO, Strang G. A simple mesh generator in MATLAB. SIAM Rev 2004;46:329–45.

[27] Cignoni P, Callieri M, Corsini M, Dellepiane M, Ganovelli F, Ranzuglia G. MeshLab: an open-source mesh processing tool. In: Proceedings of the Eurographics Italian chapter conference; 2008.

[28] Valderrabano V, Leumann A, Rasch H, Egelhof T, Hintermann B, Pagenstert G. Knee-to-Ankle mosaicplasty for the treatment of osteochondral lesions of the ankle joint. Am J Sports Med 2009;37:105S–111S.

[29] Camacho DLA, Ledoux WR, Rohr ES, Sangeorzan BJ, Ching RP. A three-dimensional, anatomically detailed foot model: a foundation for a finite element simulation and means of quantifying foot-bone position. J Rehabil Res Dev 2002;39:401–10.

[30] Telfer S, Erdemir A, Woodburn J, Cavanagh PR. Simplified versus geometrically accurate models of forefoot anatomy to predict plantar pressures: a finite element study. J Biomech 2016;49:289–94.